A rapid method for determining organic matter maturity using Raman spectroscopy: Application to Carboniferous organic-rich mudstones and coals

Henry D.G.[a,*], Jarvis I.[a], Gillmore G.[a], Stephenson M.[b]

[a] Department of Geography, Geology and the Environment, Kingston University London, Kingston upon Thames, KT1 2EE, UK
[b] British Geological Survey, Keyworth, Nottingham, NG12 5GG, UK

ABSTRACT

A simple and rapid automated Raman maturity method is calibrated using a suite of Carboniferous organic-rich mudstones and coals from the Inch of Ferryton-1 borehole in the Midland Valley of Scotland. Sediments in the borehole have been thermally matured by intrusion of a quartz dolerite sill, generating vitrinite reflectance (VR) values ranging from 0.5 to 6.0%VR$_o$. Calibration curves are tested on eight other UK wells penetrating Carboniferous shales and coals in the Midland Valley and southern Pennine Basin. The G-band full-width at half-maximum (G-FWHM) is the best Raman parameter to estimate the thermal maturity of organic matter (OM) in the oil and gas window (0.5 to 3%VR$_o$) and has a very strong correlation with VR$_o$.

1. Introduction

Raman spectroscopy has been used to track the thermal maturity of organic matter (OM) in sedimentary and metamorphic rocks (Pasteris and Wopenka, 1991; Spötl et al., 1998; Kelemen and Fang, 2001; Beyssac et al., 2002; Jehlička et al., 2003; Marshall et al., 2005; Quirico et al., 2005; Rahl et al., 2005; Schopf et al., 2005; Guedes et al., 2010; Liu et al., 2013; Muirhead et al., 2012, 2016; Aoya et al., 2010; Kouketsu et al., 2014; Zhou et al., 2014; McNeil et al., 2015; Bonoldi et al., 2016; Ferralis et al., 2016; Lünsdorf, 2016; Sauerer et al., 2017; Schito et al., 2017; Schmidt et al., 2017; Baludikay et al., 2018; Khatibi et al., 2018). Studies have had various degrees of success and results show significant inconsistencies between Raman thermal maturity parameters and vitrinite reflectance (e.g. Quirico et al., 2005; Bonoldi et al., 2016; Sauerer et al., 2017; Schmidt et al., 2017; Schito et al., 2017; Khatibi et al., 2018). This is attributed to measuring different sample types and performing different methods of spectra acquisition and processing, which can significantly impact the Raman parameters (Lünsdorf et al., 2014; Henry et al., 2018). This paper applies the method of Henry et al. (2018) that does not perform spectral deconvolution and therefore avoids processing bias and longer processing time when deriving Raman parameters. The downside of not performing deconvolution is that the parameters cannot be assigned to specific modes of vibrations, as they are a result of several different modes interacting with each other (Beyssac et al., 2002; Ferralis et al., 2016).

The aim of this study is to: (1) apply the methodology developed by Henry et al. (2018) to construct Raman vs. vitrinite reflectance calibration curves using several Raman parameters; (2) test the calibration curves on several wells that intersect Carboniferous coals and shales and; (3) determine which is the best Raman parameter to provide equivalent VR values that are similar to measured VR values for samples in the oil and gas maturity ranges (0.6–3%VR$_o$). We confirm Raman spectroscopy as being a powerful new tool for the rapid quantification of organic matter maturity in petroleum basins, with particular application to shale gas exploration.

2. Material and methods

2.1. Material

Washed and registered cuttings collected from the British Geological Survey (BGS) core store were used (Table 1, Fig. 1a). The cuttings were first analysed using Raman spectroscopy, and selected samples were subsequently prepared for vitrinite reflectance (VR) analysis; samples were selected to cross-check previously reported VR values (Raymond, 1991; Green et al., 2001; Smith et al., 2011; Andrews, 2013) and to obtain data for sample intervals where VR values were unavailable.

Table 1

Borehole samples used in this study along with depth, series /stage, rock unit and measured vitrinite reflectance (%VR$_o$).

Well (British National Grid: E, N) (Lat., Long.)	Sample No. (SSK)	Depth (m)	Series / Stage	Rock Unit	%VR$_o$	Rock type analysed
Inch of Ferryton-1	75826	24	U. Carboniferous[a]	Scottish Lower Coal Measures Fm.	0.57[a]	Coal
(NS 29078 69015)	75827	588	U. Carboniferous[a]	Upper Limestone Fm.	0.95[b]	Shale
(56.0916 N, 3.7571 W)	75828	640	U. Carboniferous[a]	Upper Limestone Fm.	0.75[b]	Coal
	75846	735	U. Carboniferous[a]	Limestone Coal Fm.	0.89[b]	Coal
	75829	838	U. Carboniferous[a]	Limestone Coal Fm.	1.00[b]	Coal
	75830	1021	U. Carboniferous[a]	Limestone Coal Fm.	1.85[b]	Coal
	75831	1064	U. Carboniferous[a]	Limestone Coal Fm.	2.23[b]	Coal
	75840	1155	U. Carboniferous[a]	Limestone Coal Fm.	3.79[a]	Coal
	75841	1170	U. Carboniferous[a]	Limestone Coal Fm.	4.03[b]	Coal
	75842	1423	U. Carboniferous[a]	Limestone Coal Fm.	6.04[b]	Coal
	75843	1487	U. Carboniferous[a]	Limestone Coal Fm.	4.28[b]	Shale
	75844	1637	L. Carboniferous[a]	Lower Limestone Fm.	2.97[b]	Coal
	75845	2057	Devonian[a]	Stratheden Group	2.21[b]	Shale
Milton of Balgonie-1	80037	305	U. Carboniferous[a]	Upper Limestone Fm.	0.48[a]	Shale
(NT 33173 99335)	80249	408	U. Carboniferous[a]	Upper Limestone Fm.	0.47[b]	Coal
(56.1820 N, 3.0781 W)	80250	489	U. Carboniferous[a]	Upper Limestone Fm.	0.65[b]	Coal
	80251	582	U. Carboniferous[a]	Limestone Coal Fm.	0.67[a]	Coal
	80272	625	U. Carboniferous[a]	Limestone Coal Fm.	nd	Coal
	80252	649	U. Carboniferous[a]	Limestone Coal Fm.	0.83[b]	Coal
	80253	704	U. Carboniferous[a]	Limestone Coal Fm.	1.95[b]	Shale
	80254	762	U. Carboniferous[a]	Limestone Coal Fm.	2.18[a]	Coal
	80255	777	U. Carboniferous[a]	Limestone Coal Fm.	3.02[b]	Coal
	80256	799	U. Carboniferous[a]	Limestone Coal Fm.	3.32[b]	Coal
	80273	805	U. Carboniferous[a]	Limestone Coal Fm.	nd	Coal
	80257	817	L. Carboniferous[a]	Lower Limestone Fm.	4.00[b]	Coal
	80258	847	L. Carboniferous[a]	Lower Limestone Fm.	2.21[a]	Shale
	80259	1030	L. Carboniferous[a]	Lower Limestone Fm.	3.74[b]	Coal
	80260	1036	L. Carboniferous[a]	Lower Limestone Fm.	3.54[b]	Coal
	80261	1082	L. Carboniferous[a]	Lower Limestone Fm.	2.11[b]	Shale
	80262	1097	L. Carboniferous[a]	Lower Limestone Fm.	2.38[b]	Shale
	80263	1125	L. Carboniferous[a]	Lower Limestone Fm.	1.44[b]	Coal
	80264	1137	L. Carboniferous[a]	Lower Limestone Fm.	1.26[a]	Coal
	80265	1195	L. Carboniferous[a]	Lower Limestone Fm.	1.56[a]	Coal
	80266	1210	L. Carboniferous[a]	Lower Limestone Fm.	1.35[b]	Coal
	80267	1222	L. Carboniferous[a]	Lower Limestone Fm.	0.75[b]	Coal
	80268	1280	L. Carboniferous[a]	Strathclyde Group	0.84[b]	Shale
	80277	1445	L. Carboniferous[a]	Strathclyde Group	0.87[b]	Shale
	80269	1484	L. Carboniferous[a]	Strathclyde Group	0.90[a]	Coal
	80278	1600	L. Carboniferous[a]	Strathclyde Group	0.90[b]	Shale
	80279	1783	L. Carboniferous[a]	Strathclyde Group	nd	Shale
	80270	1911	L. Carboniferous[a]	Strathclyde Group	1.13[b]	Shale
	80035	1966	L. Carboniferous[a]	Strathclyde Group	1.20[b]	Coal
	80271	1975	L. Carboniferous[a]	Strathclyde Group	1.26[b]	Shale
	80036	1981	L. Carboniferous[a]	Strathclyde Group	4.54[b]	Shale
Calais-3	80232	24	L. Carboniferous[a]	Lower Limestone Fm.	1.71[b]	Coal
(NT 12764 86386)	80233	30	L. Carboniferous[a]	Lower Limestone Fm.	1.62[b]	Coal
(56.0623 N, 3.4026 W)	80234	49	L. Carboniferous[a]	Lower Limestone Fm.	1.51[b]	Coal
	80235	52	L. Carboniferous[a]	Lower Limestone Fm.	1.51[b]	Coal
	80236	64	L. Carboniferous[a]	Lower Limestone Fm.	1.39[b]	Shale
	80237	66	L. Carboniferous[a]	Lower Limestone Fm.	nd	Coal
	80238	88	L. Carboniferous[a]	Strathclyde Group	1.32[b]	Shale
	80239	98	L. Carboniferous[a]	Strathclyde Group	2.03[b]	Shale
	80040	111	L. Carboniferous[a]	Strathclyde Group	nd	Coal
	80042	137	L. Carboniferous[a]	Strathclyde Group	1.44[b]	Coal
	80043	146	L. Carboniferous[a]	Strathclyde Group	1.51[b]	Shale
	80044	152	L. Carboniferous[a]	Strathclyde Group	1.68[b]	Coal
	80045	168	L. Carboniferous[a]	Strathclyde Group	2.07[b]	Shale
	80046	174	L. Carboniferous[a]	Strathclyde Group	3.80[b]	Coal
Kirk Smeaton-1	75847	250	Westphalian C[c]	Pennine Upper Coal Measures Fm.	0.55[c]	Coal
(SE 51142 16097)	75848	512	Westphalian B[c]	Pennine Middle Coal Measures Fm.	0.70[c]	Coal
(53.6389 N, 1.2280 W)	75849	758	Westphalian A[c]	Pennine Lower Coal Measures Fm.	0.80[c]	Coal
	75850	1002	Namurian[c]	Millstone Grit Group	0.90[c]	Shale
	75851	1252	Namurian[c]	Millstone Grit Group	1.20[c]	Shale
	75852	1590	Namurian[c]	Bowland Shale Fm.	1.40[c]	Shale
Gun Hill-1	75853	250	Namurian[c]	Millstone Grit Group	0.65[c]	Shale
(SJ 97230 61820)	75854	481	Namurian[c]	Bowland Shale Fm.	0.70[c]	Shale
(53.1535 N, 2.0429 W)	75855	503	Namurian[c]	Bowland Shale Fm.	1.50[c]	Shale
	75856	622	Namurian[c]	Bowland Shale Fm.	1.40[c]	Shale
	75857	839	Namurian[c]	Bowland Shale Fm.	1.10[c]	Shale
	75858	956	Namurian[c]	Bowland Shale Fm.	1.20[c]	Shale
	75859	1401	Namurian[c]	Bowland Shale Fm.	1.60[c]	Shale

Table 1 (*continued*)

Well (British National Grid: E, N) (Lat., Long.)	Sample No. (SSK)	Depth (m)	Series / Stage	Rock Unit	%VR$_o$	Rock type analysed
Gainsborough-2	75860	764	Westphalian B[c]	Pennine Middle Coal Measures Fm.	0.45[c]	Coal
(SK 81774 90785)	75861	897	Westphalian B[c]	Pennine Middle Coal Measures Fm.	0.65[c]	Shale
(53.4077 N, 0.7714 W)	75862	1089	Westphalian B[c]	Pennine Middle Coal Measures Fm.	0.60[c]	Coal
	75863	1302	Westphalian A[c]	Pennine Lower Coal Measures Fm.	0.71[c]	Shale
	75864	1797	Namurian[c]	Millstone Grit Group	0.75[c]	Shale
	75865	1844	Namurian[c]	Bowland Shale Fm.	0.80[c]	Shale
	75866	1900	Namurian[c]	Bowland Shale Fm.	0.75[c]	Shale
Duffield-1	75869	1046	Visean[d]	Bowland Shale Fm.	1.25[d]	Shale
(SK 34280 42170)						
(52.9758 N, 1.4911 W)						
Rufford-1	80051	451	Westphalian[e]	Pennine Middle Coal Measures Fm.	0.59[e]	Coal
(SK 64718 62200)	80052	499	Westphalian[e]	Pennine Middle Coal Measures Fm.	0.59[e]	Coal
(53.1530 N, 1.0337 W)	80053	748	Westphalian[e]	Pennine Lower Coal Measures Fm.	0.71[e]	Coal
	80054	1201	Tournaisian-Visean	Carboniferous Limestone Supergroup	0.79[e]	Shale
Carsington Dam Reconstruction-1	4471	39	Namurian	Bowland Shale Fm.	0.62[a]	Shale
(SK 24285 50473)						
(53.0508 N, 1.6393 W)						

Fm. = Formation. nd = not determined.
[a] VR values determined in this study.
[b] Raymond (1991).
[c] Andrews (2013).
[d] Smith et al. (2011).
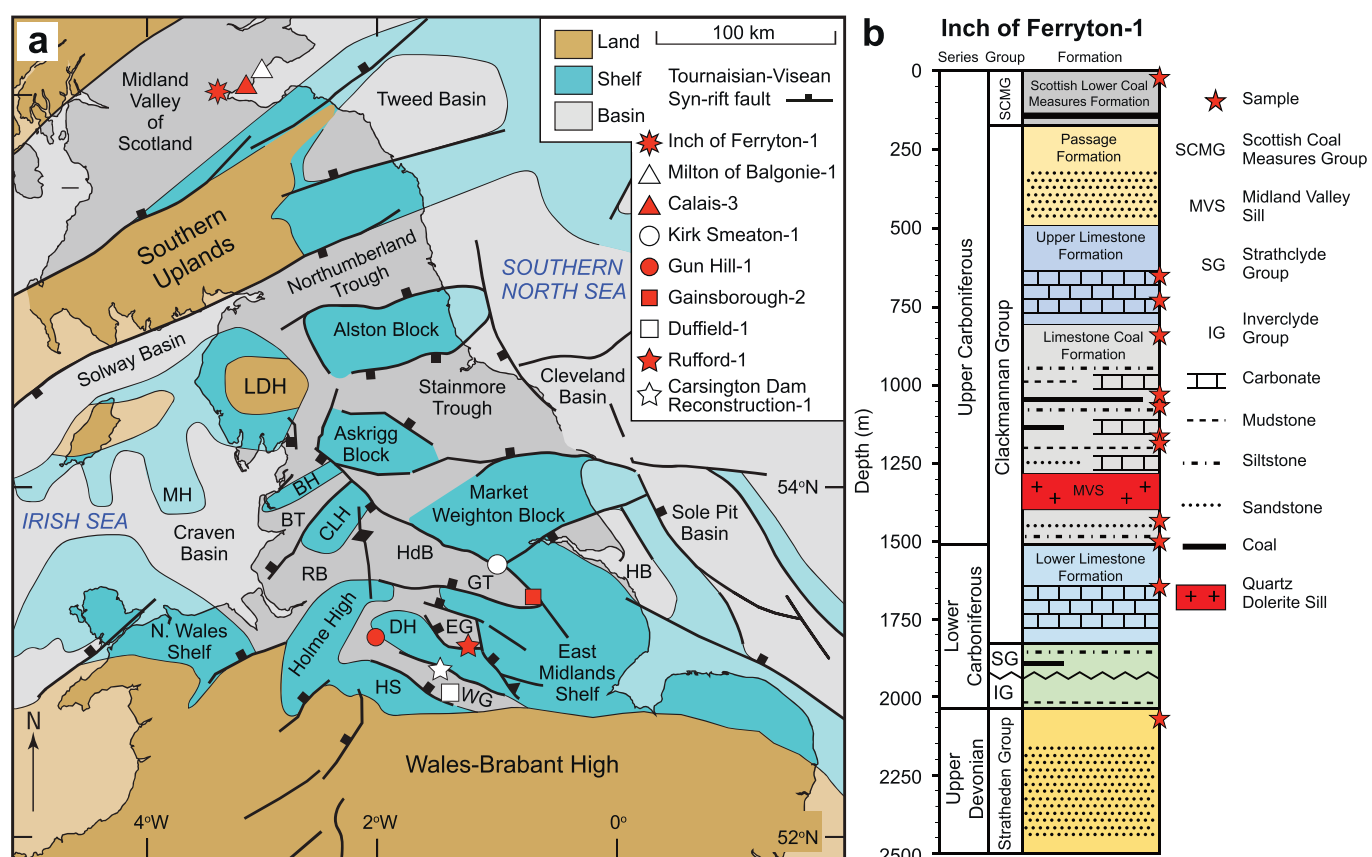[e] Green et al. (2001).

Fig. 1. (a) Geological framework of the Carboniferous and the location of the wells used in this study. Base map from Waters et al. (2009). The Pennine Basin, a complex fault-controlled mosaic of shelves and sub-basins, extends between the Southern Uplands and the Wales-Brabant High. BH–Bowland High; BT–Bowland Trough; CLH–Central Lancashire High; DH–Derbyshire High; EG–Edale Gulf; GT–Gainsborough Trough; HB–Humber Basin; HdB–Huddersfield Basin; HS–Hathern Shelf; LDH–Lake District High; MH–Manx High; WG–Widmerpool Gulf. Reproduced with the permission of the British Geological Survey ©NERC. All rights reserved. (b) Core summary of the Inch of Ferryton-1 borehole and the depths of samples used to calibrate the Raman with vitrinite reflectance. Adapted from Raymond (1991) and Monaghan (2014).

Samples from the Inch of Ferryton-1 borehole (Table 1), located in the Midland Valley of Scotland (Fig. 1), were used to correlate Raman parameters with VR$_o$ data. The well penetrates Carboniferous rocks that are similar in age to the Bowland Shale of central England, which is the main target for shale gas exploration in the UK (Andrews, 2013; Clarke et al., 2018). The Inch of Ferryton-1 borehole has an unusually wide

maturity range of 0.5 to 6.0%VR$_o$ (Table 1; Raymond, 1991), that is otherwise not available for the Bowland Shales in the UK. The OM in the Inch of Ferryton-1 has been thermally matured by a c.150 m thick quartz dolerite sill of Stephanian (late Pennsylvanian) age that was intruded into the Pendleian (late Mississippian) Limestone Coal Formation of the Clackmannan Group (Fig. 1b). There is significant literature discussing how igneous intrusions impact sediment host rocks (Dow, 1977; Raymond and Murchison, 1988; Raymond, 1991).

In summary, thermal alteration zones (aureoles) develop around the igneous intrusion; the extent of thermal aureoles is dependent on the thickness of the intrusion, the nature of the igneous rock, hydrothermal fluids and host rocks, and the degree of post-intrusion compaction, and it is typically delineated by performing vitrinite reflectance (VR) (Dow, 1977; Raymond and Murchison, 1988). VR values increase exponentially as the intrusion is approached and VR values tend to be higher above the intrusion due to the preferential upwards flow of hydrothermal fluids (Raymond and Murchison, 1988). The extent of thermal aureoles typically varies between 30 and 200% of the intrusion thickness (Dow, 1977; Aarnes et al., 2010). Therefore, by measuring VR at a distance > 200% the thickness of the intrusion, the regional background burial VR values can be estimated.

The calibration curves derived from the Inch of Ferryton-1 analyses, were applied to samples from eight additional wells (Fig. 1; Table 1). Two from the Midland Valley: Milton of Balgonie-1; Calais-3; and six from the Pennine Basin of central England: Kirk Smeaton-1; Gun Hill-1; Gainsborough-2; Duffield-1; Rufford-1; Carsington Dam Reconstruction-1. The aim was to test whether laser Raman can be used as a rapid means to reliably estimate the thermal maturity of Carboniferous rocks in the UK, with a particular focus on the maturity range relevant to shale gas exploration (0.6–3%VR$_o$). All the wells intersect Carboniferous organic-rich mudstones and coals.

The Midland Valley of Scotland and Pennine Basin in central England were both formed in response to Late Devonian and Early Mississippian back-arc extension north of the Variscan orogenic front, forming a series of interconnected NE–SW graben and half-graben structures (Fig. 1; Waters et al., 2009). These basins accumulated Carboniferous organic-rich mudstones and coals, which have been identified as proven source rocks for many of the conventional oil and gas fields in central England (Andrews, 2013) and, historically, were an important source of oil shale in the Midland Valley of Scotland (Monaghan, 2014). Both the Midland Valley and Pennine Basin suffered from extensive tholeiitic magmatism during the Late Carboniferous, which led to the intrusion of sills and dykes into Lower Carboniferous strata. These intrusions led to local thermal alteration of the surrounding strata pushing the maturity of shales and coals into and above the oil and gas windows (Raymond, 1991; Monaghan, 2014).

The Midland Valley of Scotland boreholes: Inch of Ferryton-1; Milton of Balgonie-1; and Calais-3, penetrate thick Carboniferous strata with interbedded coals, siltstones, sandstones, mudstones and carbonates with igneous intrusions. Inch of Ferryton-1 was drilled by Tricentrol in 1986 to test the conventional hydrocarbon potential of the Namurian and Dinantian sandstones (Monaghan, 2014). The well includes the Carboniferous Scottish Lower Coal Measures Formation, Clackmannan Group (Passage Formation, Upper Limestone Formation, Limestone Coal Formation, Lower Limestone Formation), Strathclyde Group and Inverclyde Group, followed by the Devonian Stratheden Group at the base (Fig. 1). The quartz-dolerite Midland Valley Sill is intruded into the Limestone Coal Formation (Namurian). Thin tuff intervals are also present below the sill. Milton of Balgonie-1 was drilled by Burmah Oil Exploration in 1984 to test the conventional hydrocarbon potential of the Earl's Sear Anticline, targeting Lower Carboniferous sandstones (Monaghan, 2014). Similar to the Inch of Ferryton-1, the Midland Valley Sill has intruded the Clackmannan Group (Namurian) with several minor tuff, lava and quartz-dolerite sills deeper in the Strathclyde Group (Visean), below. Calais-3 was an appraisal well drilled by Berkeley Resources Limited in 1986 (Monaghan, 2014). The

well intersected the Lower Limestone Formation and the Strathclyde Group. An igneous sill was encountered at the base of the well at c. 185 m depth, in the Strathclyde Group.

The remaining six wells are located in the Carboniferous Pennine Basin, an interconnected mosaic of rift basins and shelves in central England (Fig. 1). The wells are associated with interbedded coals, siltstones, sandstones, mudstones and carbonates, with some minor igneous intrusions and lavas. Kirk Smeaton-1 was a wildcat well drilled in the Gainsborough Trough by RTZ Oil and Gas Limited in 1985 (Andrews, 2013). The well encountered the Triassic–Permian Sherwood Sandstone Group (SSG), followed by the Carboniferous Pennine Coal Measures Group (Westphalian A–C), Millstone Grit Group and the Bowland Shale Formation. There is no evidence of igneous intrusions. Gun Hill-1 was drilled by D'Arcy Exploration in 1938 and is on the western flank of the Derbyshire High in the Widmerpool Gulf (Andrews, 2013). The well intersects a thick Carboniferous sequence including the Millstone Grit Group and the Bowland Shale Formation. There are also several intervals of lava flows known as the Gun Hill lava between 400 and 900 m in Visean-aged strata. Gainsborough-2 was drilled by British Petroleum in 1959 in the Gainsborough Trough (Andrews, 2013). The well intersects the Triassic–Permian Sherwood Sandstone Group, before it encounters a thick sequence of Carboniferous Pennine Coal Measures Group (Westphalian A and B), and Bowland Shale Formation. The well terminated in the Upper Bowland Shale just below a thin dolerite sill at c.1900 m. Duffield-1 was drilled by the BGS in 1966 and intersects a thick sequence of Bowland shales (Aitkenhead, 1977; Andrews, 2013). A quartz-dolerite sill intruded towards the base of the well at c. 1000 m in the Lower Bowland Shale. Rufford-1 was drilled by British Petroleum in 1986 to test the hydrocarbon potential of the Westphalian and Namurian sandstones and the Dinantian limestones (Hodge, 1986). Similar to Gainsborough-2 and Kirk Smeaton-1, the well intersects Triassic and Permian strata, followed by a thick sequence of Carboniferous Pennine Coal Measures Group (Westphalian A and B), Millstone Grit Group and the Carboniferous Limestone Supergroup. Carsington Dam Reconstruction-1 was drilled in the 1990 to assess the hydrological conditions and pressures of the reconstructed Carsington Dam following its failure in 1984 (Banyard et al., 1992; Skempton and Vaughan, 1993) and intersects Namurian Bowland Shale.

2.2. Methods

2.2.1. Laser Raman spectroscopy

Coals particles were hand-picked from the bulk samples, however, when coal particles were not present, black shale particles were selected (Table 1). The particles were analysed by a Renishaw inVia™ laser Raman instrument connected to a Leica DMLM microscope. The Rayleigh scattering was removed using an edge filter and the Raman scattering was dispersed by an 18,000 lines/mm holographic grating and detected by a charged couple device (CCD). A standard silicon wafer sample was used to calibrate the instrument by matching the 520.5 cm^{-1} band position, followed by manually aligning the laser beam with the crosshairs on the microscope. A 514.5 nm argon-ion green laser delivering c. 2 mW was used. The laser was focused through a ×50 objective, with a laser spot size of c. 2 μm. The scan range was limited to 900–2000 cm^{-1}, in order to assess the first-order region.

Where possible, up to 30 measurements of vitrinite particles from different cuttings (pieces of coal/shale) were analysed per sample depth. The data are generally normally distributed (Appendix 1). However, as the samples are cuttings, both cavings and recycled vitrinite may be present. These were identified based on the shape of the data distribution curves. Two types of data manipulation were performed: (1) isolated anomalous data points were excluded; and (2) populations of caved or reworked material (where present) were identified using histograms, and the corresponding data excluded before calculating the mean Raman parameter values to represent the true maturity of the sample (Appendix 2). The same approach is routinely
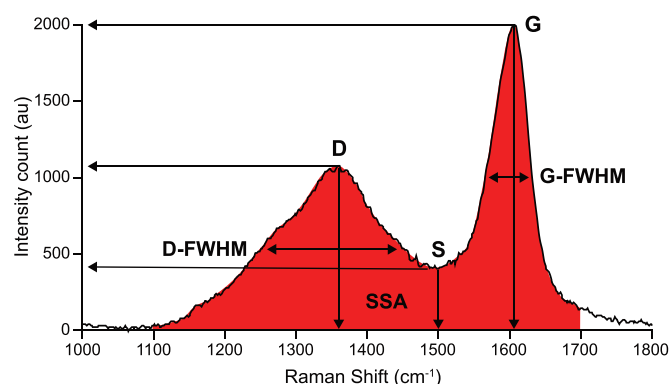
Fig. 2. Illustration of the Raman parameters. The horizontal and vertical arrows for the D (disordered, D-band), G (graphite, G-band) and S (saddle) are used to measure the height intensity and position respectively, and the double-ended arrows are used to measure the full-width half-maximum (FWHM). The SSA (scaled spectrum area) is the total area under the curve between 1100 and 1700 cm^{-1} (red shaded area). For the coloured version of this figure, the reader is referred to the web version of this article.

applied in the petroleum industry for the determination of VR values from wells (Dow, 1977; wiki.aapg.org/vitrinite_reflectance).

Renishaw WiRE 3.3 software was used to acquire spectra, which were processed in the automated Microsoft Excel® spreadsheet of Henry et al. (2018) that performs a Savitzky-Golay smoothing filter using a 21-point quadratic polynomial algorithm, a 3rd-order polynomial baseline correction, and normalizes the spectra to a common G-band height of 2000 au. The automated method is set to calculate the following Raman parameters (Fig. 2, Table 2): G-band full-width half-maximum (G-FWHM); D-band full-width half-maximum (D-FWHM); Raman band separation (RBS); R1 (D/G height ratio); saddle index (SI; G/S height ratio); and scaled spectrum area (SSA; total area under a baseline corrected curve when the G band has been normalized to an intensity count of 2000 au between 1100 and 1700 cm^{-1}). The D-FWHM cannot be calculated if the saddle height (S, Fig. 2) is above the height of the half maximum height of the D band.

2.2.2. Vitrinite reflectance

Polished blocks were prepared by embedding the same particles that were used for Raman analysis in an epoxy resin, followed by grinding and polishing according to the ISO 7404-2:2009 standard. Vitrinite reflectance (VR) was carried out using a Carl Zeiss Axio Imager.A2m microscope equipped with a halogen light source light at 546 nm and following the ISO 7404-5:2009 standard. Calibration was performed using spinel ($R_o = 0.420\%$) and gadolinium-gallium-garnet ($R_o = 1.722\%$) standards. We did not possess a standard with a higher reflectance value, therefore our own VR analyses were limited to VR_o measurements of < 1.5% (the oil window; Dow, 1977). Random reflectance measurements were taken in oil with a refractive index of 1.519. Samples selected for VR determinations were the same as those used for Raman analysis. Up to thirty measurements from the particles

selected during the hand-picking were taken per sample, where possible. The mean vitrinite reflectance results were calculated after the removal of measurements that were judged to be from cavings and/or recycled vitrinite (cf. Dow, 1977).

3. Results and discussion

3.1. Calibration

A core depth plot of the Raman parameters derived from coals and shales in this study, demonstrates that the Raman method differentiates the extent of the thermal aureole of the Midland Valley Sill in the Inch of Ferryton-1 borehole just as effectively as vitrinite reflectance (Fig. 3). The G-FWHM, SSA, R1 and D-FWHM values (Fig. 2, Table 2, Appendix 2) decrease with increasing maturity, and the saddle index (SI) and Raman band separation (RBS) increase with increasing maturity. There is a pronounced change in the values for all the Raman parameters close to the top and bottom of the sill; however, the almost vertical general depth trend lines for the SI and D-FWHM parameters (Fig. 3d, g) suggest that these parameters lack the sensitivity necessary to quantify lower thermal maturities farther away from the aureole. Note that vitrinite reflectance has a non-linear general depth trend, which is a common phenomenon when not plotted on a log scale (Dow, 1977). Whether the Raman parameters have a non-linear depth trend is uncertain, as samples deeper than c. 2050 m were not tested. The aureole symmetry in Fig. 3 for VR and G-FWHM, SSA, SI and R1 is almost identical, as the increase in maturity starts at c. 700 m; however, due to the lack of samples in the lower section, the thickness of the aureole cannot be predicted with confidence using the Raman parameters. The RBS parameter (Fig. 3e) significantly overpredicts the aureole thickness above the sill and the D-FWHM (Fig. 3g) underpredicts the width of the aureole above and below the sill.

The Raman parameters that are most sensitive to smaller incremental maturity changes in the Inch of Ferryton-1 well between maturity values of 0.6 to 3%VR_o, are the G-FWHM, SSA, SI, RBS and R1 parameters (Fig. 3b–f). Hence, these are considered to be the most reliable Raman parameters for estimating organic matter maturities in the oil and gas windows.

Raman parameters vs. vitrinite reflectance (VR_o) calibration curves (Fig. 4), indicate that the G-FWHM is the most promising parameter for maturity analysis with an R^2 of 0.96 (Fig. 4a). The G-FWHM calibration curve is steeper and the data are less scattered than the other parameters in the oil and gas windows (0.6–3%VR_o), making maturity analysis less ambiguous. Our data show similar trends to Spötl et al. (1998), Kelemen and Fang (2001), Quirico et al. (2005), Marques et al. (2009), Guedes et al. (2010), Zhou et al. (2014), Schito et al. (2017) and Schmidt et al. (2017) but differ significantly from Hinrichs et al. (2014), Bonoldi et al. (2016) and Lupoi et al. (2017) (Fig. 5a). These discrepancies are explained by differences in the data processing, particularly when performing variable deconvolution methods.

The SSA (scaled spectrum area) parameter was developed by Henry et al. (2018) and measures the total area under the curve from 1100 to 1700 cm^{-1} using the trapezoid area rule after the curve has been

Table 2

Raman parameters used to determine the maturity of organic matter examined in this study, along with the abbreviations and reference to previous studies.

| Method	Parameters	Abbreviations	References
Full-width at half-maximum (FWHM)	G	G-FWHM	e.g. Hinrichs et al. (2014); Zhou et al. (2014); Schmidt et al. (2017); Henry et al. (2018).
	D	D-FWHM	e.g. Quirico et al. (2005); Bonoldi et al. (2016); Schito et al. (2017); Henry et al. (2018).
Raman band position	G–D	RBS (Raman Band Separation)	e.g. Mumm and İnan (2016); Sauerer et al. (2017); Schmidt et al. (2017); Schito et al. (2017); Henry et al. (2018).
Ratio of Raman band height intensity	D/G	R1	e.g. Rahl et al. (2005); Schmidt et al. (2017); Sauerer et al. (2017); Roberts et al. (1995); Spötl et al. (1998); Kelemen and Fang (2001); Henry et al. (2018).
	G/S	SI (Saddle Index)	Wilkins et al. (2014); Henry et al. (2018).
Scaled spectrum area	Area $_{(1100–1700)}$	SSA	Henry et al. (2018).
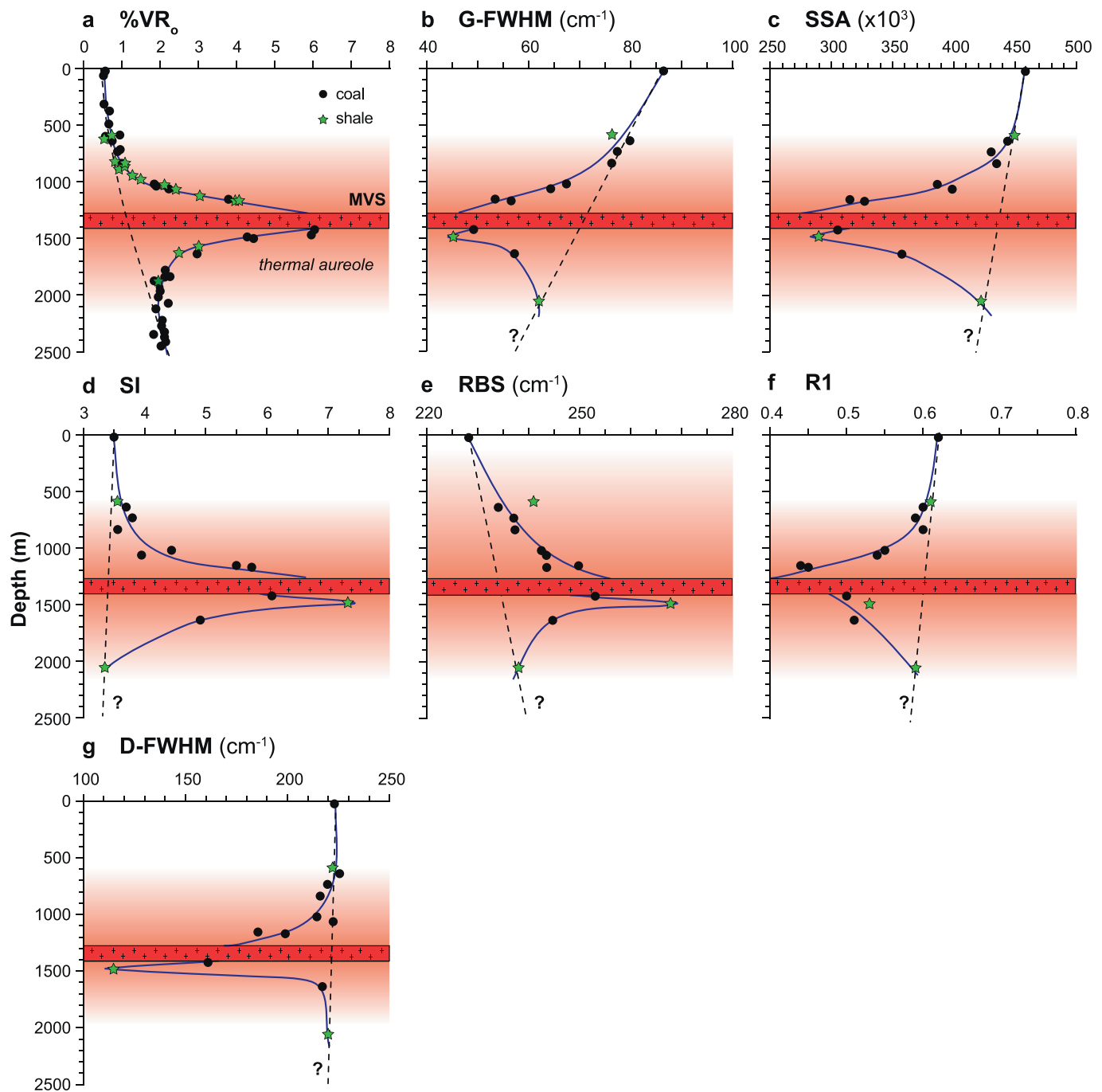
Fig. 3. Vitrinite reflectance and Raman parameters depth plots, mapping out the thermal aureole around the quartz dolerite sill (Midland Valley Sill) in the Inch of Ferryton-1 borehole. %VR$_o$ values from Raymond (1991). The red stippled area represents the vertical extent of the sill. The pink shading indicates the extent of the thermal aureole as determined from each analytical parameter. (a) Measured %VR$_o$, (b) G-FWHM, (c) SSA, (d) RBS, (e) SI, (f) R1, (g) D-FWHM. Numerical data are presented in Appendix 2. For the coloured version of this figure, the reader is referred to the web version of this article.

normalized to the same G band height of 2000 au. The SSA parameter decreases with increasing maturity and is the second-best Raman parameter with an R^2 of 0.88 (Fig. 4b). The SSA parameter has good potential to estimate the maturity of organic matter (OM) in the oil and gas windows as it has a clear negative linear trend with a lower standard deviation for VR values < 3%VR$_o$, compared to VR values > 3% VR$_o$.

The R1 parameter determined by several authors shows a trend that initially decreases and then begins to increase (Fig. 5b). The point at which the R1 ratio trend reverses varies between studies. Sauerer et al. (2017) demonstrated an increase starting at c. 1.5%VR$_o$, whereas other

authors document that the increase starts between 2.0 and 5.5%VR$_o$ (e.g. Spötl et al., 1998; Quirico et al., 2005; Zhou et al., 2014). This large variation is again attributed to variable processing methods. In this study, R1 values do not show a clear reversal of trend, but there are signs that they may start to increase at c. 4.0%VR$_o$ (Fig. 4c). Guedes et al. (2010) and Liu et al. (2013) showed a strong linear increase with substantially greater R1 values compared to the other calibration curves (Fig. 5b). Liu et al. (2013) suggested the R1 ratio is suitable for measuring the maturity of over-mature OM with VR values > 3.5%VR. Unlike the G-FWHM, Spötl et al.'s (1998) R1 calibration curve differs from this study's R1 calibration curve, as those authors' values begin to
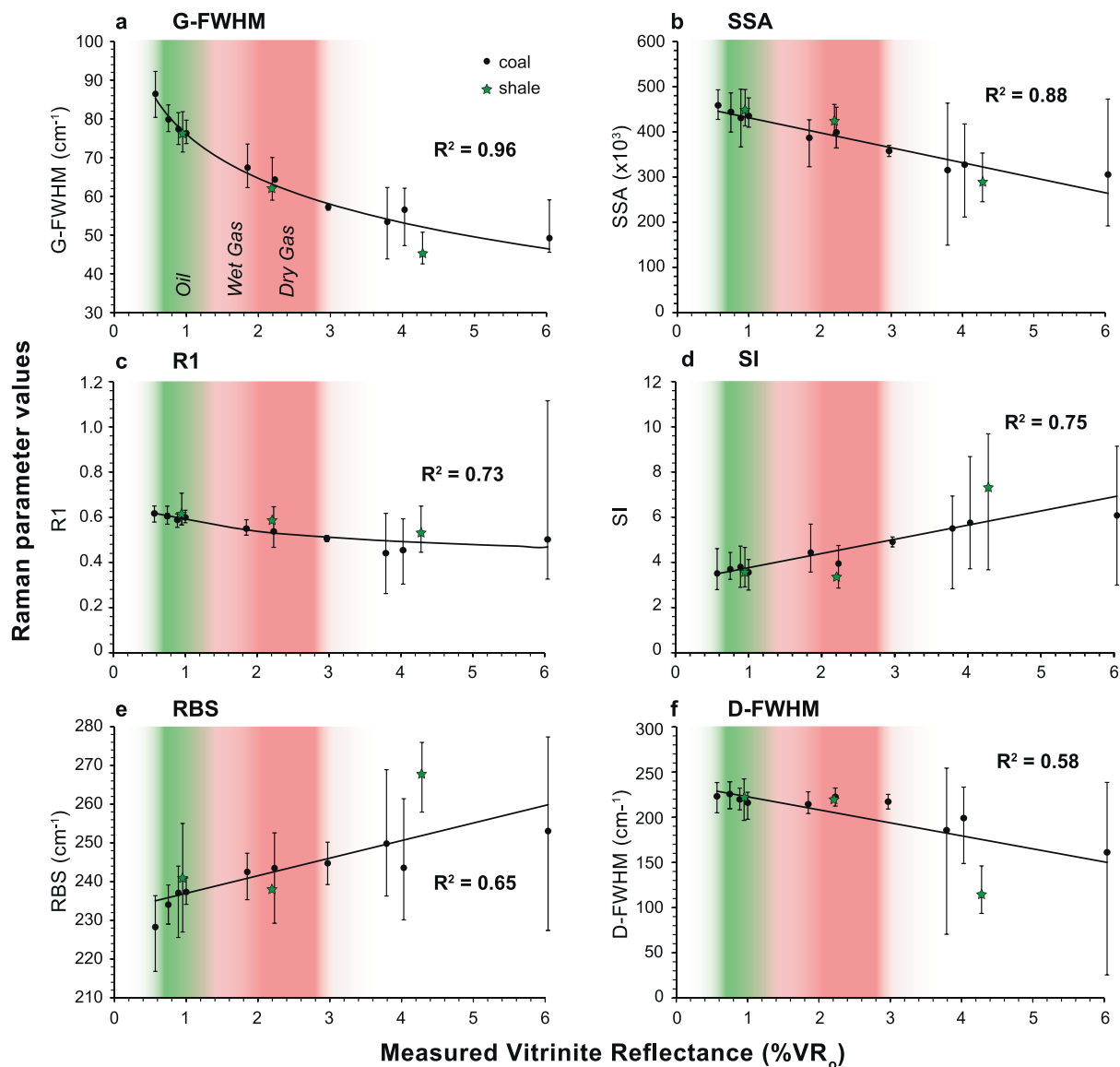
Fig. 4. Vitrinite reflectance (VR) and Raman parameter calibration curves, constructed using the values acquired from the Inch of Ferryton-1 borehole. The extent of the oil (green), wet gas (pink) and dry gas (red) windows (after Dow, 1977) is based on VR_o. The error bars are the calculated standard deviations for each sample. (a) G-FWHM, (b) SSA, (c) RBS, (d) SI, (e) R1, (f) D-FWHM. Numerical data are presented in Appendix 2. For the coloured version of this figure, the reader is reffered to the web version of this article.

increase at c. 2.5%VR (Fig. 5b).

The saddle index (SI) was first used by Wilkins et al. (2014) who integrated this parameter into a multi-linear regression equation known as the 'RaMM' technique. In this study, the SI increases with increasing maturity with an R^2 of 0.75 (Fig. 4d), in agreement with Wilkins et al. (2014).

The RBS increases linearly with increasing maturity (Figs. 4e and 5c), as the D band position shifts to lower wavenumbers (cm^{-1}) and the G band shifts to higher wavenumbers. However, the RBS values have a large standard deviation. This may lead to significant errors when using the RBS calibration curve and it should therefore not be used independently to estimate the maturity of OM. This contradicts the conclusion of Liu et al. (2013) who proposed using the RBS parameter to estimate lower maturity OM (0.5 to 3.5%VR). The large scatter for the RBS is similar to that reported by Kelemen and Fang (2001).

The D-FWHM parameter results follow a similar trend to calibration curves in the literature (Spötl et al., 1998; Kelemen and Fang, 2001; Quirico et al., 2005; Zhou et al., 2014; Figs. 4f and 5d). The values remain relatively consistent up to c. 3%VR_o and then begin to decrease.

Hinrichs et al. (2014) calibration curve is significantly different compared to other published calibration curves, particularly at low VR values. This is attributed to the deconvolution method used. Negligible variation between maturity values of 0.5 to 3%VR_o, makes the D-FWHM parameter unsuitable for determining the maturity of organic matter for the oil and gas industry.

3.2. Case study on Carboniferous samples in the UK

A blind test was conducted to estimate the equivalent VR for 78 Carboniferous samples (Fig. 1), using the G-FWHM, SSA, SI, RBS and R1 calibration curve equations (Table 3) derived from the Inch of Ferryton-1 borehole study (Appendix 2). The results are then compared to measured VR values.

3.2.1. Midland Valley sites

The Milton of Balgonie-1 results show a close correlation between %VR_o and %$_{eq}VR$ for most Raman parameters (Fig. 6a). Notably, both VR_o and Raman parameters have a sharp decrease in the VR values in
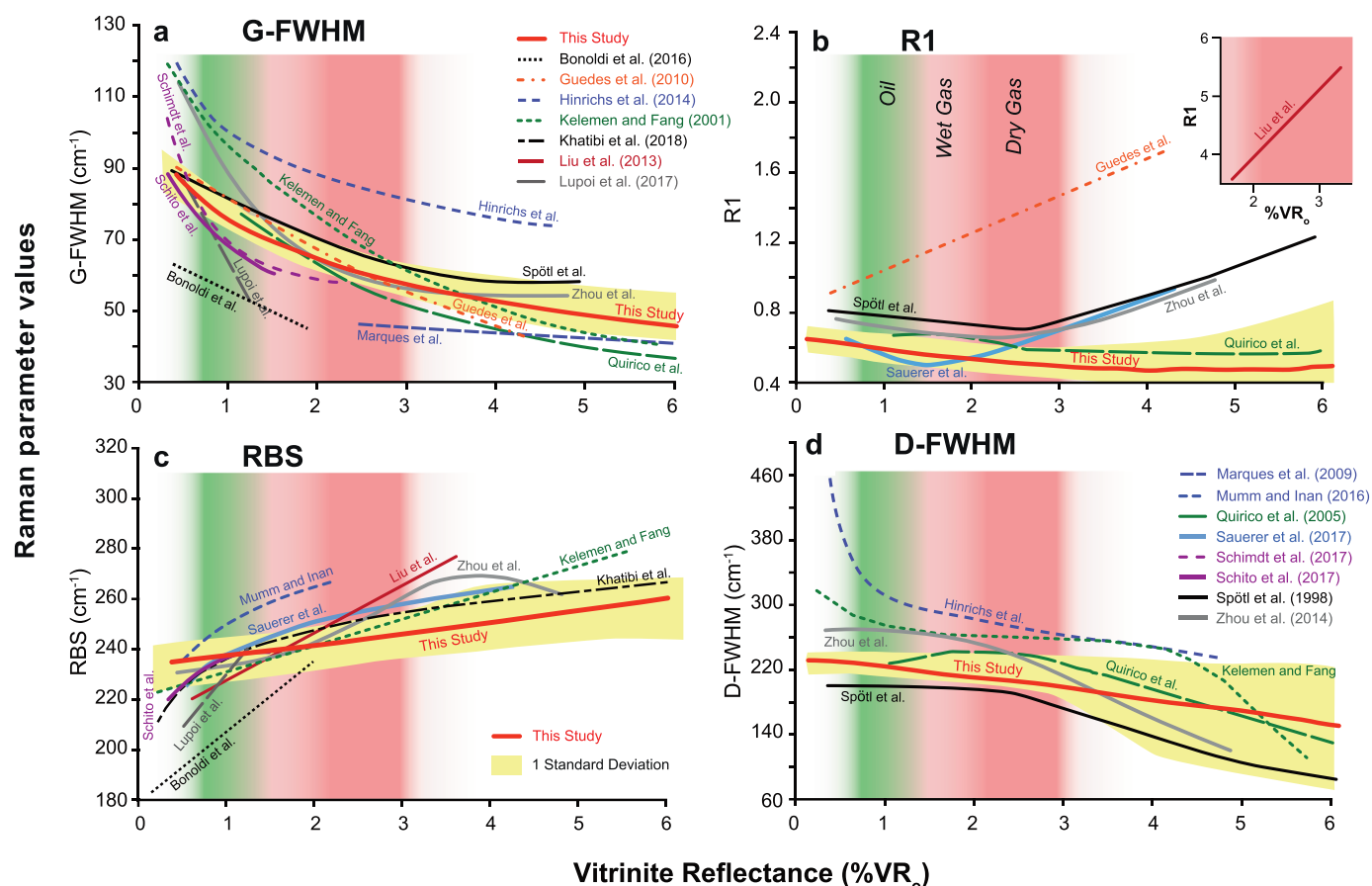
Fig. 5. Superimposed key Raman parameter calibration curves from selected publications, compared to this study. (a) G-FWHM, (b) R1, (c) RBS, (d) D-FWHM. For the coloured version of this figure, the reader is referred to the web version of this article.

Table 3
G-FWHM, SSA, RBS and SI vs. VR calibration curve equations for the maturity range 0.5 to 6%VRₒ.

Parameters	R^2	Equation
G-FWHM	0.96	$\%_{eq}VR = 85.7830385291 * EXP^{(-0.058254813 \, * \, G\text{-}FWHM)}$
SSA	0.88	$\%_{eq}VR = -0.0000264097 * SSA + 12.6257416613$
SI	0.75	$\%_{eq}VR = 1.1765899192 * SI - 2.9499539579$
R1	0.73	$\%_{eq}VR = 1945.4938205866 * EXP^{-11.6106553161 \, * \, R1)}$
RBS	0.62	$\%_{eq}VR = 0.1359255714 * RBS - 30.6210791875$

close proximity (above and below) to the quartz dolerite sill (Midland Valley Sill). This has been observed near the contact of igneous intrusions by several authors (Raymond and Murchison, 1988; Bishop and Abbott, 1995; Yao et al., 2011; Wang and Liu, 2015). Bishop and Abbott (1995) showed that the decrease starts at about 10% distance of the thickness of the dyke; in this study, the decrease in VR starts at about 10% above and 15% below the intrusion. This difference is due to more compaction above the sill, compared to below the sill. Khorasani et al. (1990) proposed two reasons for this sharp decrease in VR close to intrusions: (1) difficulty in polishing high maturity vitrinite particles; and (2) differences in molecular disordering that occurs at high heating rates near the sill. Our study suggests that polishing is not the reason for this phenomenon, as the laser Raman analysed unpolished rock chips. It is concluded that the apparent decrease in maturity near the intrusion is a result of natural thermochemical reactions that occur at a distance of < 15% thickness of the intruded dolerite sill.

The Raman spectra of the samples taken close to the Midland Valley Sill in the Milton of Balgonie-1 well are significantly different from the

Raman spectra at a greater distance from the sill (Fig. 6aiii). Similar spectra have been reported by Rantitsch et al. (2014) and Morga et al. (2015) from coke samples, with R1 ratios > 1.00. The coke spectra are similar to spectrum 3 in Fig. 6aiii (sample SSK 80259), which is substantially different compared to the R1 ratio measured in coals (< 0.80). This is also observed in the Inch of Ferryton-1 well and is accompanied by a sharp decrease in VR values in very close proximity of the sill.

The G-FWHM, SSA, SI and RBS $\%_{eq}VR$ results have a strong correlation with VR data, whereas the R1 parameter has $\%_{eq}VR$ that are shifted to higher values. However, anomalous Raman and VR results below the sill at depths > 1200 m (circled in Fig. 6a) are present and could be due to the complex stratigraphy that includes multiple extruded lava flows and thin quartz dolerite sills in the lower section (Raymond, 1991), although the possibility of unrecognised cavings cannot be excluded.

The %VRₒ and $\%_{eq}VR$ values follow a similar trend for the Calais-3 borehole (Fig. 6b). The G-FWHM, SSA, SI and RBS parameters yield $\%_{eq}VR$ values that are closest to VRₒ, whereas the R1$\%_{eq}VR$ data are again shifted to higher values. The strange concave VR maturity trend for Calais-3 (Fig. 6b) is most likely the result of a previously overlying sill that has been eroded, combined with the basal dolerite sill below 190 m. The Raman parameters also show an increase in maturity values between 57 and 82 m, which suggests that there may be another igneous intrusion nearby (Fig. 6biii), that has not been picked out by the VR results. Although an igneous intrusion has not been identified previously at that level, the well report indicates evidence of baking at c.95 m (Aitkenhead, 1977), implying that an igneous body may be present.
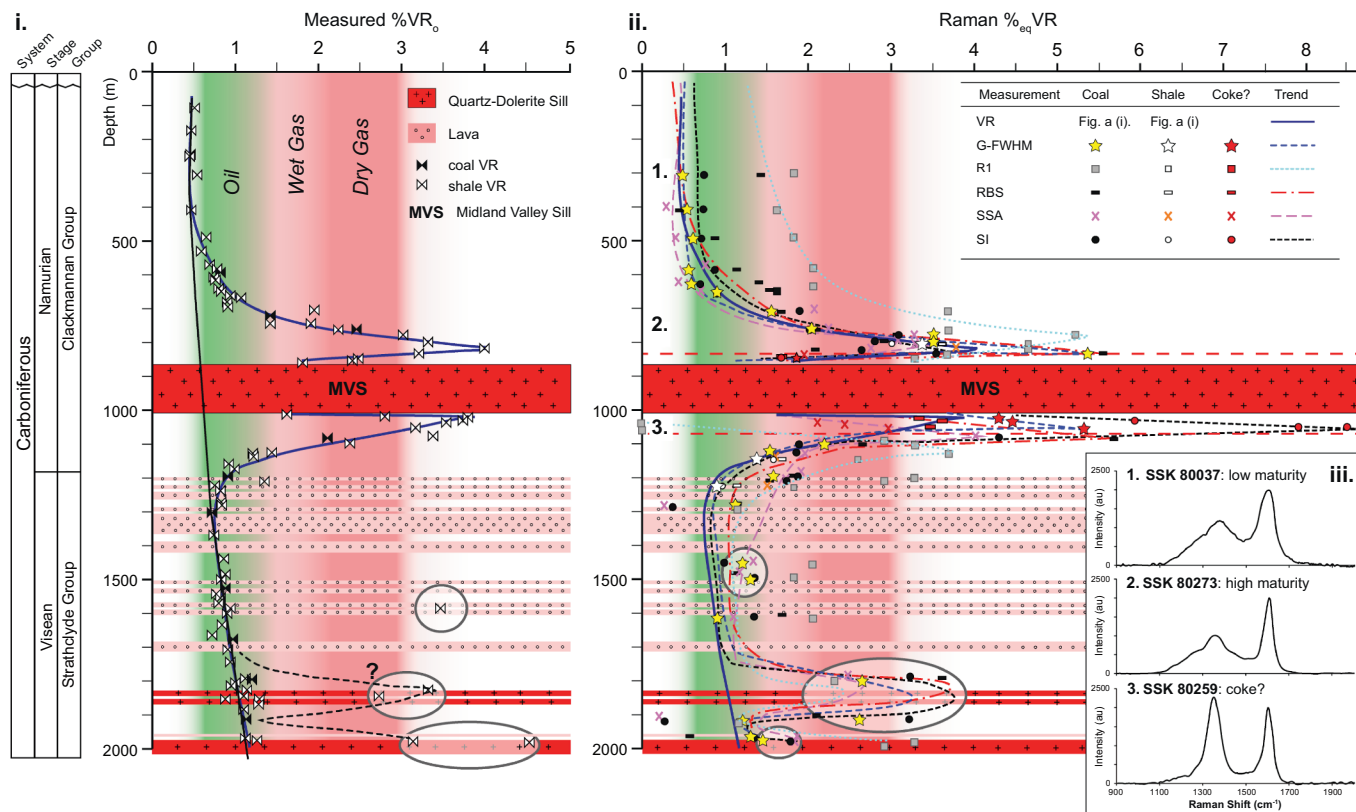
3.2.2. Southern Pennine Basin sites

One sample was analysed for the Duffield-1 well, from a depth of c.1100 m (Fig. 6c). The G-FWHM, SSA, RBS and SI1%$_{eq}$VR values are in good agreement with %VR$_o$; R1 values are again too high. The sharp increase in %VR$_o$ is attributed to a sill near the base of the well (Andrews, 2013).
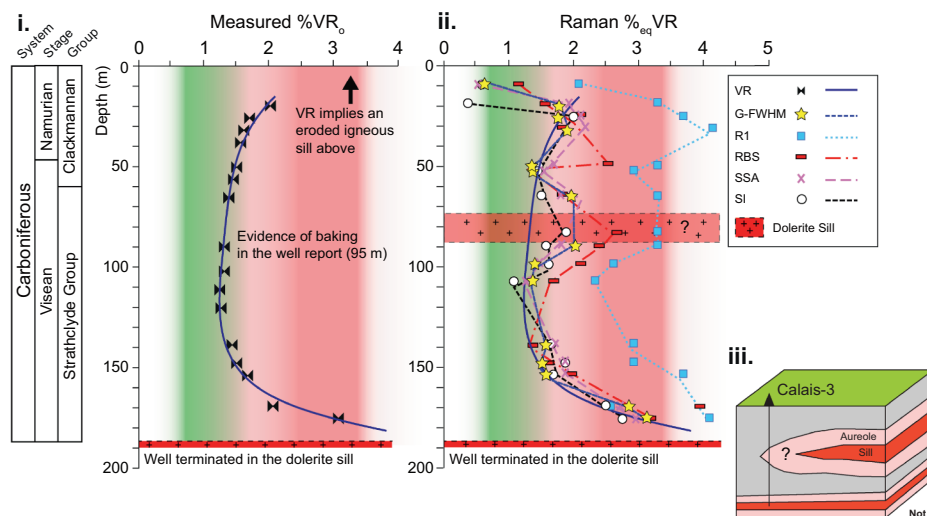
The VR data for Gainsborough-2 fluctuates between 0.4 and 0.7% VR$_o$ down to 1800 m and then there is an increase to 1.1 %VR$_o$ just below the sill at the base of the well (1900 m) (Andrews, 2013). An increase in the G-FWHM, SSA, RBS and SI1 %$_{eq}$VR is also evident

(Fig. 6d). The G-FWHM data have the best correlation with %VR$_o$. The G-FWHM %$_{eq}$VR and %VR$_o$ results are very similar for the Rufford-1 well, whereas, the SSA, RBS, SI and R1 %$_{eq}$VR data show substantial discrepancies (Fig. 6e). At 1300 m in Gainsborough-2 there is a negative value for the SI parameter, which occurs when the background fluorescence curvature is underestimated. This leads to a higher saddle height and a lower SI ratio number, resulting in a lower than expected maturity or a negative value. This issue could be addressed with further spectrum processing, but this negates the objective of having an automated approach. It is advised to reject these spurious data points, as is
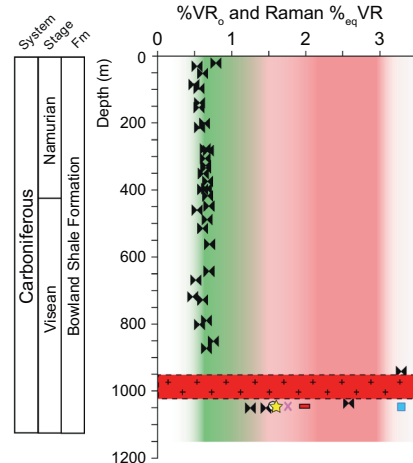

Fig. 6. Core depth plots vs. maturity measurements for the several wells estimated using the G-FWHM, SSA and RBS calibration curve equations in Table 3. Midland Valley: (a) Milton of Balgonie-1; (b) Calais-3. Southern Pennine Basin: (c) Kirk Smeaton-1; (d) Gainsborough-2; (e) Gun Hill-1; (f) Rufford-1; (g) Duffield-1. Numerical data are presented in Appendix 2. For the coloured version of this figure, the reader is referred to the web version of this article.
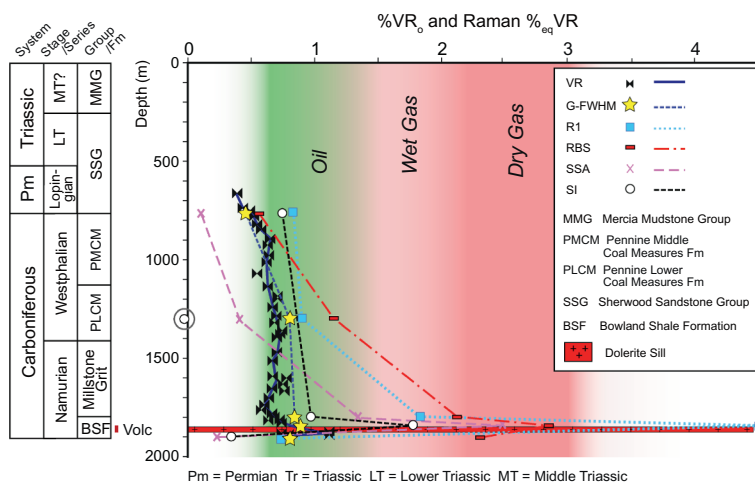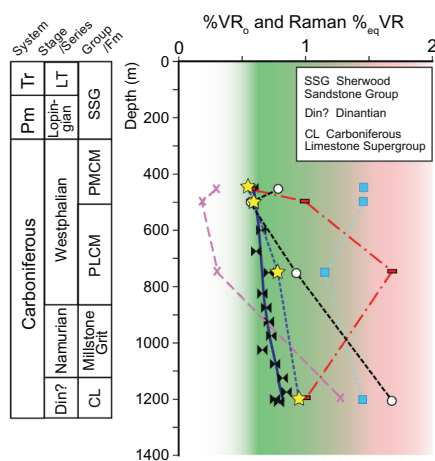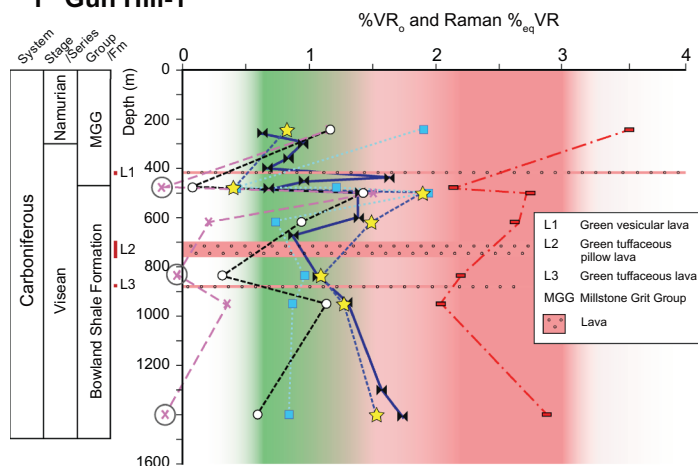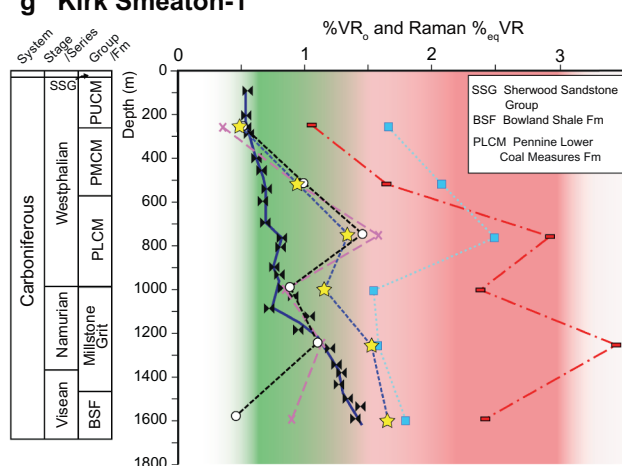
d Gainsborough-2

e Rufford-1

f Gun Hill-1

g Kirk Smeaton-1

Fig. 6. (*continued*)

common practice when reviewing vitrinite reflectance and Rock-Eval pyrolysis data sets.

There is substantial scatter in %VR$_o$ for the Gun Hill-1 well above 700 m depth, which is replicated by the G-FWHM, SSA, SI and RBS %$_{eq}$VR profiles, (Fig. 6f). The RBS substantially overestimates the maturity of the samples but follows the same trend as the other parameters (Fig. 6f). The SSA fails to generate acceptable %$_{eq}$VR values, as some of the results are negative. The reason for this is that the background correction has underestimated the curvature of the background fluorescence, and therefore increased the total area under the curve to the baseline, resulting in very low or negative maturity results. G-FWHM %$_{eq}$VR has the best correlation with measured VR values. The results for the Kirk Smeaton-1 well show a smooth %VR$_o$ profile that increases with depth (Fig. 6g). The G-FWHM, SSA, RBS and SI1 %$_{eq}$VR profiles follow the same trend but with higher VR values and greater variance. The G-FWHM %$_{eq}$VR values are closest to the %VR$_o$ data and the R1 and RBS parameters overestimate the VR values.

Fig. 7 is a summary of %VR$_o$ vs. %$_{eq}$VR for the G-FWHM, SSA, SI, R1 and RBS parameters for all the samples analysed. Overall, G-FWHM has the tightest correlation with %VR$_o$ with an R^2 of 0.84, and can successfully generate %$_{eq}$VR values that are similar to measured %VR$_o$ values, as the trend line lies almost on top of the 1:1 line (Fig. 7a). The SSA and SI %$_{eq}$VR parameters correlate well with %VR$_o$, yielding R^2 values of 0.75 and 0.71, respectively (Fig. 7b-c), but have greater scatter than the G-FWHM Raman parameter. The R1 and RBS calibration curves have the greatest scatter for maturities in the oil and gas

windows (0.6–3.0%VR), and they both overestimate %$_{eq}$VR for maturities < 3.0%VR$_o$.

The G-FWHM parameter has the greatest potential to be used as a universal maturity proxy, however there is large scatter for higher maturities (Fig. 7a). This is because the calibration curve is non-linear and flattens out for higher maturities, therefore small changes in the G-FWHM for higher maturity samples give large differences in %$_{eq}$VR (Fig. 4a). This is not the case for maturities < 3.5%VR$_o$ as the calibration curve is steep and linear. The other calibration curves may be used to confirm the results, but they should not be used independently, as there is significant scatter. The Pennine Basin and Midland Valley of Scotland samples also follow a similar maturity path for the G-FWHM Raman parameter (Fig. 7a), however the Pennine Basin data have greater scatter than the Midland Valley of Scotland results for the rest of the Raman parameters (Fig. 7b-e). This is likely caused by more intense and variable background fluorescence in the Pennine Basin samples compared to those from the Midland Valley of Scotland, which tends to have a greater impact on the SSA, SI, R1 and RBS Raman parameters.

4. Conclusion

Raman parameter calibration curves constructed using samples from the Inch of Ferryton-1 borehole have been successfully tested on Carboniferous organic-rich sediments from the Midland Valley of Scotland and the southern Pennine Basin, central England. The Raman parameter with the strongest correlation with measured vitrinite
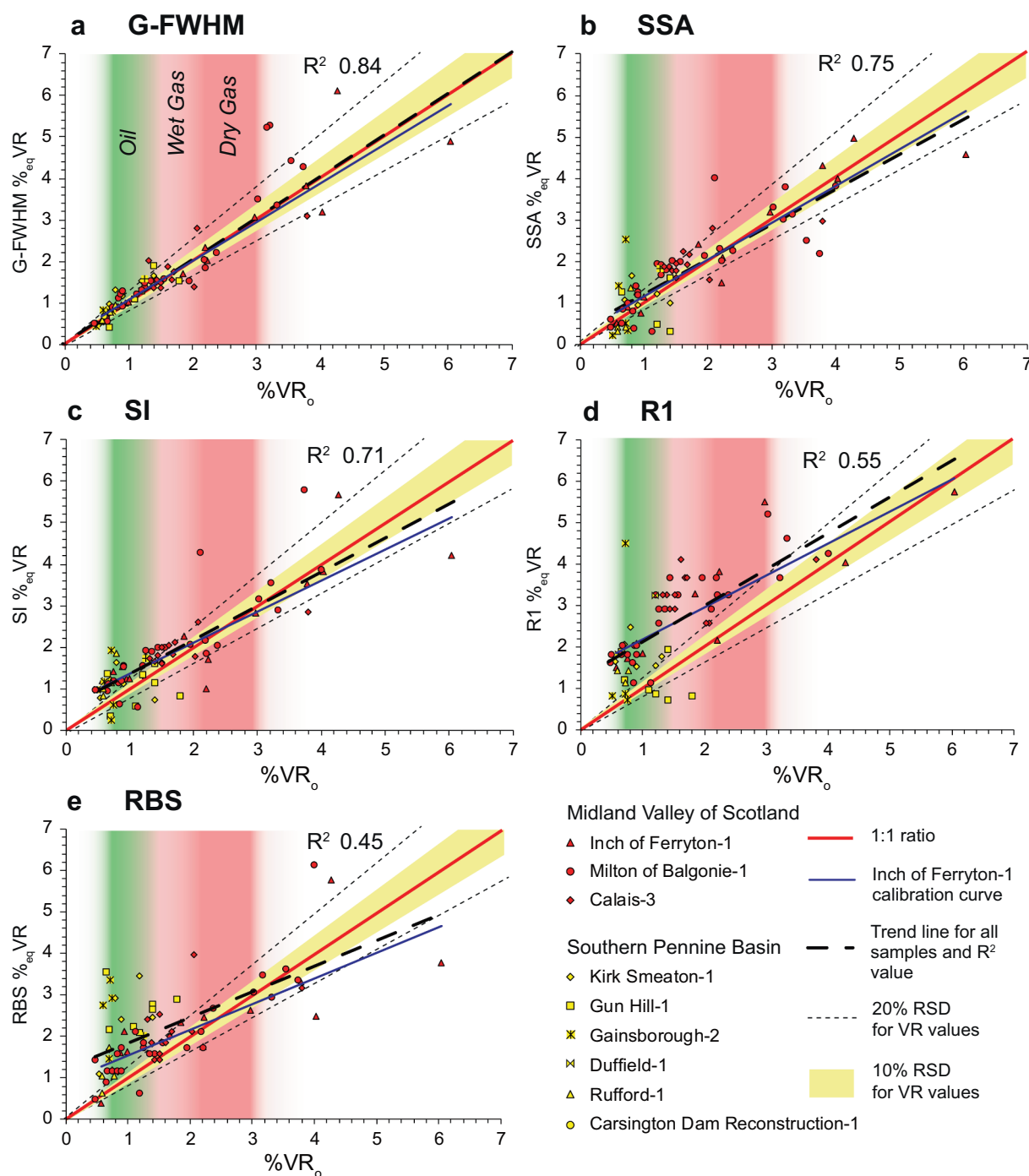
Fig. 7. Comparison of the %eqVR and %VRo for 78 Carboniferous rock samples from the UK. (a) G-FHWM. (b) SSA. (c) SI. (d) R1. (e) RBS. Red data points: Midland Valley of Scotland. Yellow data points: southern Pennine Basin. The yellow area represents an average 10% standard deviation for VR values, according to Barker (1996). For the coloured version of this figure, the reader is referred to the web version of this article.

reflectance (%VRo) is the G-FWHM, which can successfully generate similar VR equivalent values in the oil and gas windows (0–3.0%VRo). Due to the non-linear nature of the G-FWHM calibration curve, un-reliable results may be derived for samples that have a maturity > 3.5% VRo.

Maturity measurements can be acquired rapidly on well cuttings, with the potential to be performed on-site using a portable Raman in-strument early in an oil and/or gas fields life cycle. The SSA, RBS, R1, D-FWHM and SI Raman parameters may be used alongside the G-FWHM parameter to better constrain the maturity of OM, but they

should not be used independently due to large scatter in the results.

The G-FWHM calibration curve has the potential to be used uni-versally, but further work must be performed to refine the calibration curve and test it in a wider range of sedimentary basins around the world. Testing the method in areas of known VR suppression and/or retardation caused by the presence of Type II hydrogen-rich macerals, lithological variation, and overpressurized basins would also be in-structive; as well as testing laser Raman in scenarios where VR cannot be measured, such as pre-Devonian and deep marine shales where vi-trinite particles are absent or rare.

Acknowledgements

Appendix A. Supplementary data

Supplementary data to this article can be found online at https://doi.org/10.1016/j.coal.2019.01.003.

References

Aarnes, I., Svensen, H., Connolly, J.A.D., Podladchikov, Y.Y., 2010. How contact metamorphism can trigger global climate changes: modeling gas generation around igneous sills in sedimentary basins. Geochim. Cosmochim. Acta 74, 7179–7195.

Aitkenhead, N., 1977. Report of borehole at Duffield, Derbyshire. Bull. Geol. Surv. Great Brit. 59, 1–36.

Andrews, I.J., 2013. The Carboniferous Bowland Shale Gas Study: Geology and Resource Estimation. British Geological Survey for Department of Energy and Climate Change, London, UK, pp. 64.

Aoya, M., Kouketsu, Y., Endo, S., Shimizu, H., Mizukami, T., Nakamura, D., Wallis, S., 2010. Extending the applicability of the Raman carbonaceous material geothermometer using data from contact metamorphic rocks. J. Metamorph. Geol. 28, 895–914.

Baludikay, B., François, C., Sforna, M., Beghin, J., Cornet, Y., Storme, J., Fagel, N., Fontaine, F., Littke, R., Baudet, D., Delvaux, D., Javaux, E., 2018. Raman microspectroscopy, bitumen reflectance and illite crystallinity scale: comparison of different geothermometry methods on fossiliferous Proterozoic sedimentary basins (DR Congo, Mauritania and Australia). Int. J. Coal Geol. 191, 80–94.

Banyard, J.K., Coxon, R.E., Johnston, T.A., 1992. Carsington reservoir - reconstruction of the dam. Proc. Inst. Civ. Eng. Civ. Eng. 92, 106–115.

Barker, C.E., 1996. A comparison of vitrinite reflectance measurements made on wholerock and dispersed organic matter concentrate mounts. Org. Geochem. 24, 73–111.

Beyssac, O., Goffé, B., Chopin, C., Rouzaud, J.N., 2002. Raman spectra of carbonaceous material in metasediments: a new geothermometer. J. Metamorph. Geol. 20, 859–871.

Bishop, A.N., Abbott, G.D., 1995. Vitrinite reflectance and molecular geochemistry of Jurassic sediments: the influence of heating by Tertiary dykes (Northwest Scotland). Org. Geochem. 22, 165–177.

Bonoldi, L., Di Paolo, L., Flego, C., 2016. Vibrational spectroscopy assessment of kerogen maturity in organic-rich source rocks. Vib. Spectrosc. 87, 14–19.

Clarke, H., Turner, P., Bustin, R.M., Riley, N., Besly, B., 2018. Shale gas resources of the Bowland Basin, NW England: a holistic study. Petrol. Geosci. 24, 287–322.

Dow, W.G., 1977. Kerogen studies and geological interpretations. J. Geochem. Explor. 7, 79–99.

Ferralis, N., Matys, E.D., Knoll, A.H., Hallmann, C., Summons, R.E., 2016. Rapid, direct and non-destructive assessment of fossil organic matter via micro-Raman spectroscopy. Carbon 108, 440–449.

Green, P.F., Thomson, K., Hudson, J.D., 2001. Recognition of tectonic events in undeformed regions: contrasting results from the Midland Platform and East Midlands Shelf, Central England. J. Geol. Soc. 158, 59–73.

Guedes, A., Valentim, B., Prieto, A.C., Rodrigues, S., Noronha, F., 2010. Micro-Raman spectroscopy of collotelinite, fusinite and macrinite. Int. J. Coal Geol. 83, 415–422.

Henry, D.G., Jarvis, I., Gillmore, G., Stephenson, M., Emmings, J., 2018. Assessing lowmaturity organic matter in shales using Raman spectroscopy: Effects of sample preparation and operating procedure. Int. J. Coal Geol. 191, 135–151.

Hinrichs, R., Brown, M.T., Vasconcellos, M.A.Z., Abrashev, M.V., Kalkreuth, W., 2014. Simple procedure for an estimation of the coal rank using micro-Raman spectroscopy. Int. J. Coal Geol. 136, 52–58.

Hodge, A., 1986. Rufford-1 (L K/30-6) – Geological Completion Report. BP.

Jehlička, J., Urban, O., Pokorný, J., 2003. Raman spectroscopy of carbon and solid bitumens in sedimentary and metamorphic rocks. Spectrochim. Acta A Mol. Biomol. Spectrosc. 59, 2341–2352.

Kelemen, S.R., Fang, H.L., 2001. Maturity trends in Raman spectra from kerogen and coal. Energy Fuel 15, 653–658.

Khatibi, S., Ostadhassan, M., Tuschel, D., Gentzis, T., Bubach, B., Carvajal-Ortiz, H., 2018. Raman spectroscopy to study thermal maturity and elastic modulus of kerogen. Int. J. Coal Geol. 185, 103–118.

Khorasani, G.K., Murchison, D.G., Raymond, A.C., 1990. Molecular disordering in natural cokes approaching dyke and sill contacts. Fuel 69, 1037–1046.

Kouketsu, Y., Mizukami, T., Mori, H., Endo, S., Aoya, M., Hara, H., Nakamura, D., Wallis, S., 2014. A new approach to develop the Raman carbonaceous material geothermometer for low-grade metamorphism using peak width. Island Arc 23, 33–50.

Liu, D., Xiao, X., Tian, H., Min, Y., Zhou, Q., Cheng, P., Shen, J., 2013. Sample maturation calculated using Raman spectroscopic parameters for solid organics: Methodology and geological applications. Chin. Sci. Bull. 58, 1285–1298.

Lünsdorf, N.K., 2016. Raman spectroscopy of dispersed vitrinite - methodical aspects and correlation with reflectance. Int. J. Coal Geol. 153, 75–86.

Lünsdorf, N.K., Dunkl, I., Schmidt, B.C., Rantitsch, G., von Eynatten, H., 2014. Towards a higher comparability of geothermometric data obtained by Raman spectroscopy of carbonaceous material. Part I: Evaluation of biasing factors. Geostand. Geoanal. Res. 38, 73–94.

Lupoi, J.S., Fritz, L.P., Parris, T.M., Hackley, P.C., Solotky, L., Eble, C.F., Schlaegle, S., 2017. Assessment of thermal maturity trends in Devonian–Mississippian source rocks using Raman spectroscopy: limitations of peak-fitting method. Front. Energy Res. 5, 24.

Marques, M., Suárez-Ruiz, I., Flores, D., Guede, A., Rodrigues, S., 2009. Correlation between optical, chemical and micro-structural parameters of high-rank coals and graphite. Int. J. Coal Geol. 77, 377–382.

Marshall, C., Javaux, E., Knoll, A., Walter, M., 2005. Combined micro-Fourier transform infrared (FTIR) spectroscopy and micro-Raman spectroscopy of Proterozoic acritarchs: a new approach to Palaeobiology. Precambrian Res. 138, 208–224.

McNeil, D.H., Schulze, H.G., Matys, E., Bosak, T., 2015. Raman spectroscopic analysis of carbonaceous matter and silica in the test walls of recent and fossil agglutinated foraminifera. AAPG Bull. 99, 1081–1097.

Monaghan, A.A., 2014. The Carboniferous Shales of the Midland Valley of Scotland: Geology and Resource Estimation. British Geological Survey for Department of Energy and Climate Change, London, UK, pp. 96.

Morga, R., Jelonek, I., Kruszewska, K., Szulik, W., 2015. Relationship between quality of coals, resulting cokes, and micro-Raman spectral characteristics of these cokes. Int. J. Coal Geol. 144 (145), 130–137.

Muirhead, D.K., Parnell, J., Taylor, C., Bowden, S.A., 2012. A kinetic model for the thermal evolution of sedimentary and meteoritic organic carbon using Raman spectroscopy. J. Anal. Appl. Pyrolysis 96, 153–161.

Muirhead, D.K., Parnell, J., Spinks, S., Bowden, S.A., 2016. Characterization of organic matter in the Torridonian using Raman spectroscopy. In: Brasier, A.T., Mcilroy, D., Mcloughlin, N. (Eds.), Earth System Evolution and Early Life: A Celebration of the Work of Martin Brasier. Vol. 448. pp. 71–80 Geol. Soc. London Spec. Publ.

Mumm, A.S., İnan, S., 2016. Microscale organic maturity determination of graptolites using Raman spectroscopy. Int. J. Coal Geol. 162, 96–107.

Pasteris, J.D., Wopenka, B., 1991. Raman spectra of graphite as indicators of degree of metamorphism. Can. Mineral. 29, 1–9.

Quirico, E., Rouzaud, J., Bonal, L., Montagnac, G., 2005. Maturation grade of coals as revealed by Raman spectroscopy: progress and problems. Spectrochim. Acta A Mol. Biomol. Spectrosc. 61, 2368–2377.

Rahl, J.M., Anderson, K.M., Brandon, M., Fassoulas, C., 2005. Raman spectroscopic carbonaceous material thermometry of low-grade metamorphic rocks: calibration and application to tectonic exhumation in Crete, Greece. Earth Planet. Sci. Lett. 240, 339–354.

Rantitsch, G., Bhattacharyya, A., Schenk, J., Lünsdorf, N.K., 2014. Assessing the quality of metallurgical coke by Raman spectroscopy. Int. J. Coal Geol. 130, 1–7.

Raymond, A.C., 1991. Carboniferous Rocks of the Eastern and Central Midland Valley of Scotland: Organic Petrology, Organic Geochemistry and Effects of Igneous Activity. Unpublished PhD Thesis. University of Newcastle upon Tyne, pp. 597.

Raymond, A.C., Murchison, D.G., 1988. Development of organic maturation in the thermal aureoles of sills and its relation to sediment compaction. Fuel 67, 1599–1608.

Roberts, S., Tricker, P.M., Marshall, J.E.A., 1995. Raman spectroscopy of chitinozoans as a maturation indicator. Org. Geochem. 23, 223–228.

Sauerer, B., Craddock, P.R., Aljohani, M.D., Alsamadony, K.L., Abdallah, W., 2017. Fast and accurate shale maturity determination by Raman spectroscopy measurement with minimal sample preparation. Int. J. Coal Geol. 173, 150–157.

Schito, A., Romano, C., Corrado, S., Grigo, D., Poe, B., 2017. Diagenetic thermal evolution of organic matter by Raman spectroscopy. Org. Geochem. 106, 57–67.

Schmidt, J.L., Hinrichs, R., Araujo, C.V., 2017. Maturity estimation of phytoclasts in strew mounts by micro-Raman spectroscopy. Int. J. Coal Geol. 173, 1–8.

Schopf, J.W., Kudryavtsev, A.B., Agresti, D.G., Czaja, A.D., Wdowiak, T.J., 2005. Raman imagery: a new approach to assess the geochemical maturity and biogenicity of permineralized Precambrian fossils. Astrobiology 5, 333–371.

Skempton, A.W., Vaughan, P.R., 1993. The failure of Carsington Dam. Géotechnique 43, 151–173. https://doi.org/10.1680/geot.1993.43.1.151.

Smith, N., Turner, P., Williams, G., 2011. UK data and analysis for shale gas prospectivity. In: Vining, B.A., Pickering, S.C. (Eds.), Petroleum Geology: From Mature Basins to New Frontiers. Petroleum Geology Conference Series 7, Geol. Soc. London, pp. 1087–1098.

Spötl, C., Houseknecht, D.W., Jaques, R.C., 1998. Kerogen maturation and incipient graphitization of hydrocarbon source rocks in the Arkoma Basin, Oklahoma and Arkansas: a combined petrographic and Raman spectrometric study. Org. Geochem. 28, 535–542.

Wang, R., Liu, G., 2015. Variations of concentration and composition of polycyclic aromatic hydrocarbons in coals in response to dike intrusion in the Huainan coalfield in eastern China. Org. Geochem. 83 (84), 202–214.

Waters, C.N., Waters, R.A., Barclay, W.J., Davies, J.R., 2009. A Lithostratigraphic Framework for Carboniferous Successions of Southern Great Britain (Onshore) British Geological Survey, Research Report (2009) (RR/09/01). pp. 60.

Wilkins, R.W.T., Boudou, R., Sherwood, N., Xiao, X., 2014. Thermal maturity evaluation from inertinites by Raman spectroscopy: the 'RaMM' technique. Int. J. Coal Geol. 128, 143–152.

Yao, Y.B., Liu, D.M., Huang, W.H., 2011. Influences of igneous intrusions on coal rank, coal quantity and adsorption capacity in Hongyang, Handan and Huaibei coalfields, North China. Int. J. Coal Geol. 88, 135–146.

Zhou, Q., Xiao, X., Pan, L., Tian, H., 2014. The relationship between micro-Raman spectral parameters and reflectance of solid bitumen. Int. J. Coal Geol. 121, 19–25.